Article

Water Deficit Caused by Land Use Changes and Its Implications on the Ecological Protection of the Endorheic Dalinor Lake Watershed in Inner Mongolia, China

Longfeng Wang [1], Wenpeng Li [1,*], Yuejun Zheng [1], Xuefei Zhang [2], Fuqiang Yuan [3,4,*] and Xia Wu [5,*]

[1] China Institute of Geo-Environmental Monitoring, Beijing 100081, China; wanglf.14b@igsnrr.ac.cn (L.W.)
[2] China National Institute of Standardization, Beijing 100088, China
[3] Institute of Hydrogeology and Environmental Geology, Chinese Academy of Geological Sciences, Shijiazhuang 050061, China
[4] School of Resources and Environmental Engineering, Hefei University of Technology, Hefei 230009, China
[5] Beijing Water Science Technology Institute, Beijing 100048, China
* Correspondence: liwenpeng@mail.cgs.gov.cn (W.L.); yuanfuqiang@mail.cgs.gov.cn (F.Y.); wux.16b@igsnrr.ac.cn (X.W.); Tel.: +86-10-8113-4866 (W.L.); +86-10-8113-4819 (F.Y.); +86-010-68731771 (X.W.)

Abstract: Dalinor Lake, the second-largest endorheic salt lake in Inner Mongolia, has shown a shrinking trend given the lack of a significant decrease in precipitation (PRE). Based on high-spatial-resolution datasets, we employed a linear regression model, Theil–Sen median trend analysis, the Mann–Kendall test, and a land use transfer matrix to identify the spatio-temporal distribution and trends of PRE and actual evapotranspiration (AET) at the watershed scale during 2001–2019; then, the water deficit (WD) caused by land use changes in different surface lithology zones was analyzed. The results showed that the annual PRE and WD of the Dalinor Lake watershed showed insignificant upward trends, while the annual AET showed a significant upward trend. Spatially, about 89% of the watershed showed a significant upward trend for AET, while 12% showed a weak significant upward trend for PRE. The WDs of the aeolian sand zone and the sand, gravel, and silt accumulation zone were most heavily affected by the new increased land use from 2001 to 2019, accounting for 43.14% and 25.56% of the total WD of the watershed, respectively. Specifically, the WD of the aeolian sand zone caused by the new increased grassland and farmland in 2019 accounted for 41.92% and 18.52% of the total WD of the zone, respectively. The WD of the sand, gravel, and silt accumulation zone caused by the new increased grassland and farmland in 2019 accounted for 37.07% and 35.59% of the total WD of the zone, respectively. The WD caused by the new increased land use was increased by 7.78 million m^3 in 2019 compared with the corresponding land use type in 2001, which would decrease the water yield. It is necessary to strengthen the protection of regional forest ecosystems in the granite and terrigenous clastic rock zone; standardize pasture management and reduce farmland reclamation in the sand, gravel, and silt accumulation zone, the aeolian sand zone, and the basalt platform zone; and reduce unnecessary impervious land construction in the aeolian sand zone.

Keywords: land use changes; water surplus and deficit; surface lithology; Dalinor Lake watershed

1. Introduction

Extensively distributed in arid and semiarid regions, endorheic lakes are sensitive and vulnerable to climate change and human activities [1]. The endorheic lake dynamic is controlled by the watershed hydrological cycle under the changing environment and is directly influenced by water budget status. Specifically, precipitation (PRE) controls the inflow of water, actual evapotranspiration (AET) is the main way of water consumption in arid and semi-arid areas, and land use/cover is the result of the joint action of nature and humans on the land surface. The indicator of water surplus and deficit is the difference between PRE and AET, which is the comprehensive characterization of the land use/cover, water inflow, and water outflow. It constitutes an important part of water resource management.

The spatial heterogeneity of PRE and AET makes it difficult to observe their distribution accurately. Traditional PRE observations are mainly focused on weather stations and hydrological stations based on rain gauges and ground-based radar. AET observations are mainly carried out using a pan [2], lysimeter [3], liquid flow method [4], Bowen ratio method [5,6], eddy correlation [7], flux tower [8], or large aperture scintillator [9]. PRE can only be measured by the above-mentioned traditional observation methods at the point scale, and AET at the tens-of-meters scale. Although the evapotranspiration scale measured by a single-hole, large-aperture scintillometer can reach 200 m–10 km, the cost is high. In recent years, satellite remote sensing technology has become an effective way to obtain long-term regional PRE and AET due to its wide coverage, periodicity, and timeliness, especially with the development of the Google Earth Engine (GEE). At present, the commonly used PRE datasets are mainly based on ground observation data, satellite retrieval datasets, and assimilation and reanalysis datasets. AET datasets include satellite retrieval datasets, reanalysis datasets, land surface model datasets, and empirical amplification datasets based on point-scale observations.

The spatial heterogeneity of terrestrial ecosystems needs high-spatial-resolution data to study their spatio-temporal dynamics and mechanisms. At present, the PRE datasets with high spatial resolution ($\leq$1 km scale) or high temporal resolution ($\leq$1-month scale) at home and abroad mainly include the global high-resolution climate dataset released by WorldClim [10], the annual spatial interpolation dataset of meteorological elements in China released by the Resource and Environmental Science and Data Center of the Chinese Academy of Sciences (CAS) [11], the 1 km resolution dataset of monthly PRE in China released by China Scientific Data [12], the HRLT 1 km resolution daily dataset of PRE in China released by Earth System Science Data (ESSD) [13], the 1 km resolution dataset of monthly PRE in China released by the National Earth System Science Data Center [14], etc. AET datasets with high spatial resolution ($\leq$1 km scale) and high temporal resolution ($\leq$1-month scale) mainly include the MODIS MOD16A2 dataset released by the National Aeronautics and Space Administration (NASA) [15], the SSEBop_V4 dataset based on the operational simplified surface energy model released by the United States Geological Survey (USGS) [16,17], the Synthesis of Global AET dataset released by CAS [18], the PML_V2 land AET and total primary productivity dataset released by CAS [19], etc. The spatial patterns and dynamic changes in land use/cover have great significance to solve the issues of global and regional environmental evolution and sustainable development. At present, high-spatial-resolution land use/cover datasets commonly used include the 30 m resolution CLCD_v01 dataset for China released by Wuhan University [20], GlobeLand30 released by the National Basic Geographic Information Center [21], GLC_FCS30 released by CAS [22], CNLUCC (30 m) released by CAS [23], etc.

Dalinor Lake is a typical endorheic lake in the eastern Inner Mongolia agro-pastoral ecotone, which is an important habitat for seasonal bird migration. The Dalinor Lake watershed has the characteristics of a special physical geographic environment, a complex geological structure, and a fragile ecosystem, and is closely related to groundwater (GW) [24]. The surface area of Dalinor Lake has shown a shrinking trend given the lack of a significant decrease in PRE in recent years, which has attracted widespread attention [25,26]. The lake surface area changes are mainly caused by the water budget status at the watershed scale in the changing environment. The watershed's PRE variation caused by climate change affects the inflow of water, and the watershed's land use/cover change caused by human activities affects the outflow of water. Quantitatively analyzing the water surplus and deficit caused by the land use changes at the watershed scale is the basis of supporting a harmonious and healthy ecosystem, which can have implications for the ecological protection of the Dalinor Lake watershed. Previous studies on the Dalinor Lake watershed mainly focused on the lake area or lake level changes, the spatio-temporal distribution of hydro-meteorological factors, and greenness, as well as its influencing factors at the regional or watershed scale [27–32]. Ecological protection suggestions have been proposed [32,33], but they rarely consider surface lithology zones.

In this study, based on high-spatial-resolution remote sensing datasets, we used linear regression, Theil–Sen median trend analysis, the Mann–Kendall test, and a land use transfer matrix to identify the spatio-temporal distribution and trends of PRE, AET, and water deficit (WD), and then analyze the WD caused by land use changes in different surface lithology zones from the perspective of water balance, and discuss implications for the Dalinor Lake watershed from the perspective of eco-environmental geology.

2. Materials and Methods

2.1. Study Area

Dalinor Lake is the second-largest endorheic salt lake in Inner Mongolia, formed by a basalt weir in the northwest on the basis of the tectonic dammed lake formed during the subsidence of a faulted watershed. It lies in the western Hexigten Banner, and is located at the junction of the major landforms of the southern end of the Greater Khingan Mountains, the central part of the Inner Mongolia Plateau, and the northern edge of the Otindag Desert.

The Dalinor Lake watershed is approximately 4196 km^2 (Figure 1), and belongs to the temperate continental monsoon climate zone, with the characteristics of a dry climate, strong evapotranspiration, and low rainfall. There are mainly four rivers that flow into Dalinor Lake, namely the GongGeEr River, the LiangZi River, the ShaLi River, and the Haolai River. The annual surface inflow of the Dalinor Lake watershed was 40 million m^3 in the past decade. Groundwater and spring recharge the lake from the south, with a relatively large flow of approximately 115 million m^3 annually (Zhen et al., 2014) [25].
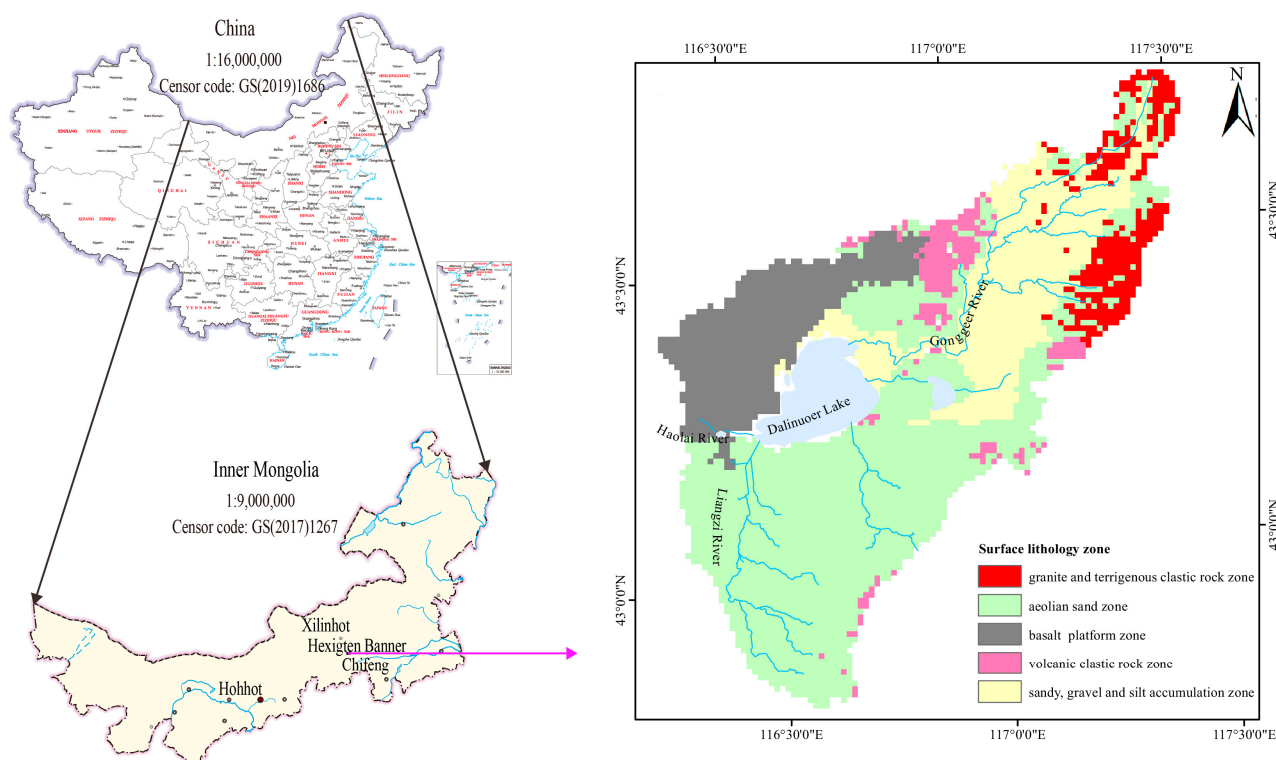

Figure 1. Sketch map of the location of the study watershed with the main rivers and surface lithology zones. The map was revised from the Chinese Standard Map (http://bzdt.ch.mnr.gov.cn/, accessed on 9 April 2023).

The surface lithology of the Dalinor Lake watershed mainly includes an aeolian sand zone, a sandy gravel silt zone, a basalt zone, a granite and terrigenous clastic rock zone, and a volcanic clastic rock zone, with areas of 2329 km^2, 950 km^2, 734 km^2, 328 km^2, and 224 km^2, respectively (Figure 1). The aeolian sand zone mostly lies in the southern area of Dalinor Lake, and is partly distributed in the eastern and northeastern areas of Dalinor Lake. The sand, gravel, and silt accumulation zone lies in the valley area of the

middle reaches of the GongGeEr River. The basalt platform zone lies in the northwestern part of the Dalinor Lake watershed. The granite and terrigenous clastic rock zone lies in the northeastern part of the Dalinor Lake watershed with middle and low mountainous distribution, and is the headwater of the GongGeEr River. The volcanic clastic rock zone lies in the basalt platform zone and the sand, gravel, and silt accumulation zone. The GW types of the Dalinor Lake watershed mainly include pore water in unconsolidated rocks, basalt cave fissure–pore water in unconsolidated rocks, basalt cave fissure water–basalt volcanic cone group, magmatic fissure water, and pore–fissure water in clastic rocks, which are described in detail in a previously published paper [24].

2.2. Data and Processing

The remote sensing datasets used in this study are described below. The PRE data from 2001 to 2019, at a resolution of 1000 m, were sourced from the National Earth System Science Data Center (http://www.geodata.cn/ (accessed on 1 April 2022)). AET data from 2001 to 2019, at a resolution of 30 m, were from the PML_V2 land AET dataset and downloaded from the GEE platform (https://developers.google.com/earth-engine/datasets/catalog/CAS_IGSNRR_PML_V2, accessed on 9 April 2022). In this study, annual data were obtained based on the downloaded remote sensing datasets using RStudio and R statistical language. Land use/land cover data for the Dalinor Lake watershed in 2001 and 2019, at a resolution of 30 m, were from CLCD_v01 and downloaded from the China Land Cover Dataset (http://doi.org/10.5281/zenodo.4417810, accessed on 9 April 2022). The land use types in 2019 included forest, grassland, farmland, wetland, waters, barren land, and impervious land, accounting for 4.57%, 87.32%, 2.75%, 0.01%, 4.34%, 0.80%, and 0.21% of the total land use, respectively.

2.3. Methods

2.3.1. Linear Regression Model

To study the temporal variation characteristics of the factors, linear regression is an effective and simple trend analysis tool. The linear regression can not only analyze the temporal variation characteristics of factors at the whole watershed scale, but also at each grid scale [34,35]. The following linear regression calculation Equations (1) and (2) are used at the whole watershed scale and each grid scale, respectively.

$$Y = a \cdot X + b \tag{1}$$

$$\mathrm{Slo}pe = \frac{n \times \sum\limits_{i=1}^{n} (i \times F_i) \sum\limits_{i=1}^{n} i \sum\limits_{i=1}^{n} F_i}{n \times \sum\limits_{i=1}^{n} i^2 (\sum\limits_{i=1}^{n} i)^2} \tag{2}$$

In Equation (1), X is the independent variable, i.e., the years. Y is the dependent variable, i.e., the factors. b is the intercept, and a is the regression slope. In Equation (2), Slope refers to the annual time series varies, i.e., the inclination rate. n is the length of the time series. F_i represents the factor values of years i. When $\mathrm{Slo}pe \succ 0$, the factor presents a rising trend; otherwise, the factor displays a decreasing trend. The contributed R package terra [36] was used to analyze the temporal variation characteristics of factors at the whole watershed scale and at each grid scale.

2.3.2. Theil-Sen Median Trend Analysis and the Mann–Kendall Test

The Theil–Sen median trend analysis is a robust trend statistical method [37–39] that can be effectively combined with the Mann–Kendall test. The combination has been gradually used to analyze the long time series of factors reflecting the variation in trends of each pixel [40,41]. In theory, the Theil–Sen median trend analysis calculates the median slopes between all $n(n - 1)/2$ pair-wise combinations of the time series data. It is based on non-parametric statistics and is particularly effective for the estimation of trends in small

series [39]. The slope of the Theil–Sen median can represent the increase or decrease in the selected factors over the 19 years between 2001 and 2019 on a pixel scale. It is calculated by

$$S_{\text{factor}} = median(\frac{factor_j - factor_i}{j - i}), \quad 2001 \le i \prec j \le 2019 \tag{3}$$

In Equation (3), S_{factor} refers to the Theil–Sen median, and $factor_i$ and $factor_j$ represent the factor values of years i and j. When $S_{\text{factor}} \succ 0$, the factor presents a rising trend; otherwise, the factor displays a decreasing trend.

The Mann–Kendall test measures the significance of a trend. It is a non-parametric statistical test and it has the advantage that samples do not need to obey certain distributions, and it is free from the interference of outliers [42,43]. It has been widely applied to analyze the trends and variations at pixel scale with hydrological and meteorological time series. The calculation equation is as follows:

$$Z = \begin{cases} \frac{S-1}{\sqrt{s(S)}}, & S \succ 0 \\ 0, & S = 0 \\ \frac{S+1}{\sqrt{s(S)}}, & S \prec 0 \end{cases} \tag{4}$$

$$S = \sum_{j=1}^{n-1} \sum_{i=j+1}^{n} \text{sgn}(factor_j - factor_i) \tag{5}$$

$$\text{sgn}(factor_j - factor_i) = \begin{cases} 1, & factor_j - factor_i \succ 0 \\ 0, & factor_j - factor_i = 0 \\ -1, & factor_j - factor_i \prec 0 \end{cases} \tag{6}$$

$$s(S) = \frac{n(n-1)(2n+5)}{18} \tag{7}$$

In Equations (4)–(7), $factor_i$ and $factor_j$ represent the factor values of the pixels i and j; n is the length of the time series; sgn is a sign function; the Z statistic is valued in the range of $(-\infty, +\infty)$. A given significance level, $|Z| > u_{1-\alpha/2}$, signifies that the times series shows significant variations in the level of α. Generally, the value of α is 0.05. In this study, we chose $\alpha = 0.05$, meaning we measured the significance of the factors trend from 2001 to 2019 on the pixel scale at a confidence level of 0.05. The contributed R packages terra [36] and trend [44] were used to implement the Theil–Sen Median trend analysis and the Mann–Kendall test.

2.3.3. Land Use Transfer Matrix

The transition matrix [45,46], a classic method for LUCC detection, was employed to explore the dynamics of LUCC in the Dalinor Lake watershed. In regard to the pair of compared datasets, an extended transition matrix was constructed. Raster maps reflecting the initial and subsequent times were overlaid in ArcGIS software to produce a matrix providing the land use change areas according to the categorical transition between two time points. The land use transfer rate and change intensity between different land use types was calculated by the following formula:

$$S_{ij} = \begin{bmatrix} S_{11} & S_{12} & \dots & S_{1n} \\ S_{11} & S_{12} & \dots & S_{1n} \\ \dots & \dots & \dots & \dots \\ S_{11} & S_{12} & \dots & S_{1n} \end{bmatrix}, \quad D_j = \sum_{i=1}^{n} S_{ij} - S_{jj} \tag{8}$$

where S_{ij} is the area converted from land use type i to type j; D_j represents the increased area of type j during the study period.

2.3.4. Water Surplus and Deficit

PRE and AET are the processes of water exchange in the vertical direction between the land surface and the atmosphere. PRE is the generalized water resource; AET is the main way of water consumption. In this study, based on the difference between PRE and AET, the water surplus and deficit were calculated using Equation (9).

$$H_d = ET - PRE \tag{9}$$

where H_d is the water surplus and deficit. AET and PRE were calculated based on each land use type at pixel scale. When $H_d > 0$, it indicates a water deficit, and it will use GW to make up for the water shortage. When $H_d < 0$, it indicates water surplus. The excess PRE will flow into rivers as runoff or be converted into GW, forming narrow water resources, which will maintain socioeconomic development and keep the ecosystem healthy [47].

3. Results and Discussion

3.1. Spatio-Temporal Distribution and Trends for PRE, AET, and WD

3.1.1. Precipitation

As shown in Figure 2, the trend of the annual PRE in the Dalinor Lake watershed fluctuated between 247 mm/a and 416 mm/a from 2001 to 2019, with an average of 318 mm/a. From 2001 to 2019, annual PRE showed a slowly increasing trend in fluctuation, with an increase rate of 3.42 mm/a, but not statistically significant ($p > 0.05$). The variation coefficient of annual PRE was 0.16, indicating moderate inter-annual fluctuation. From the spatial distribution of the PRE inclination rate (Figure 3), the spatial variation is relatively low, ranging from 0.286 mm/10 a to 0.468 mm/10 a. From southwest to northeast, the temporal trend of annual PRE showed an increasing trend. High values in the range of 0.37–0.47 mm/10 a lie in the headwater region of the GongGeEr River.
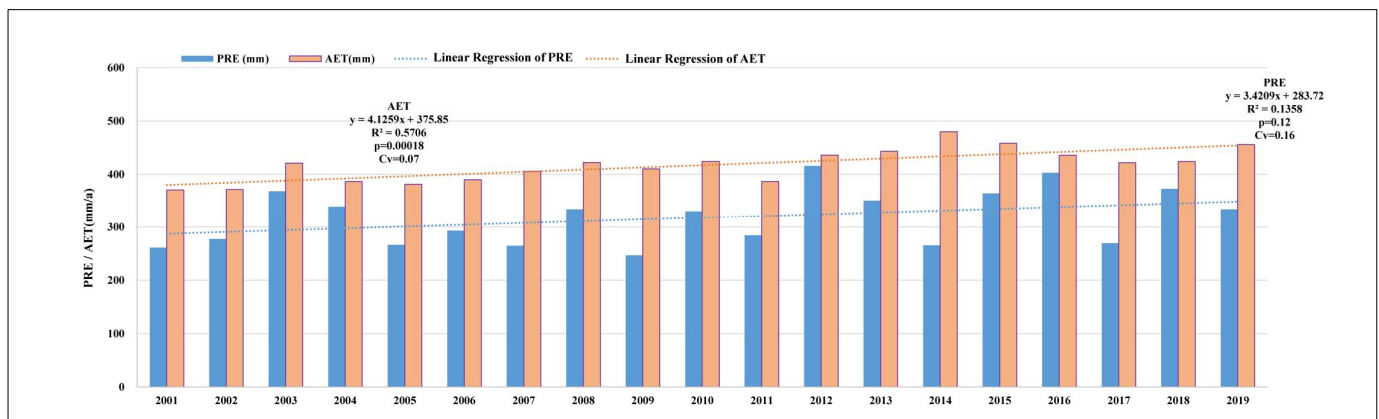

Figure 2. Inter-annual change in PRE and AET in the Dalinor Lake watershed from 2001 to 2019.

As shown in Figure 4a, the spatial distribution of average annual PRE from 2001 to 2019 showed strong spatial variations. The high-value region lies in the northeast and the low-value region in the northwest. The distribution of average annual PRE was between 220 and 345 mm, which was mainly distributed in the ranges of 296–325 mm and 326–345 mm, accounting for 54.02% and 31.72%, respectively. The average annual PRE range from 296 mm to 325 mm was mainly distributed in the northwest. As shown in Figure 5a, the spatial distribution of the annual PRE variation trends of the Dalinor Lake watershed from 2001 to 2019 showed an upward trend, especially in the headwater region of the GongGeEr River and the southeast part of Dalinor Lake, but about 88% of the whole watershed was not statistically significant, and only about 12% of the whole watershed near the middle reaches of the GongGeEr River showed a weak significant upward trend (Figure 4b).
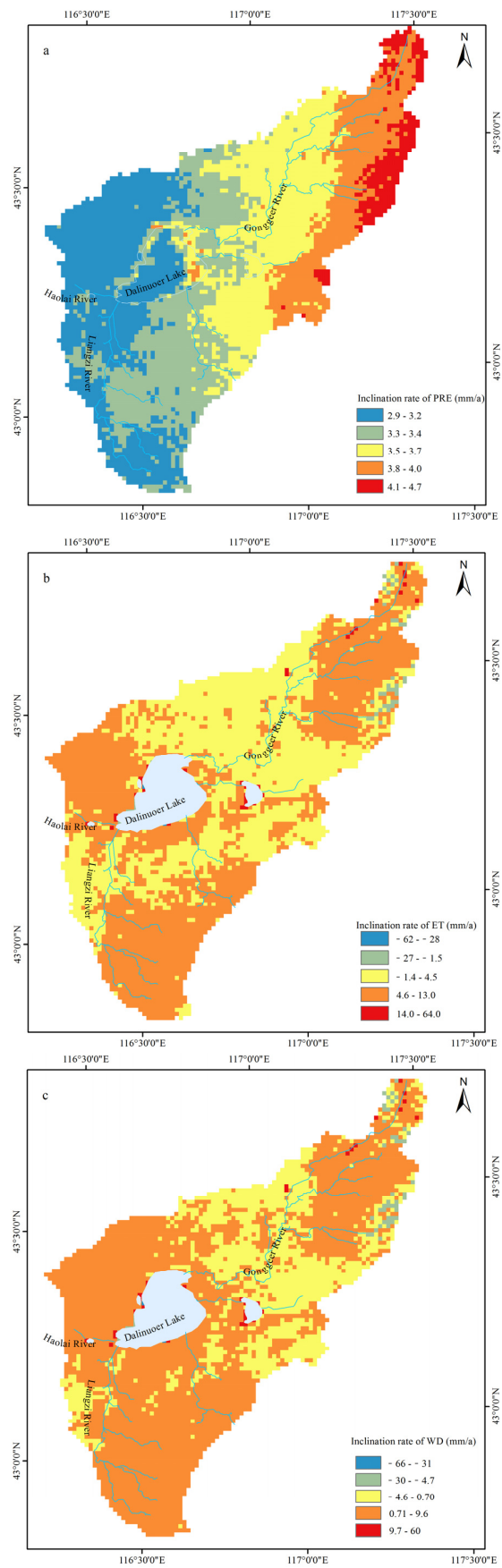
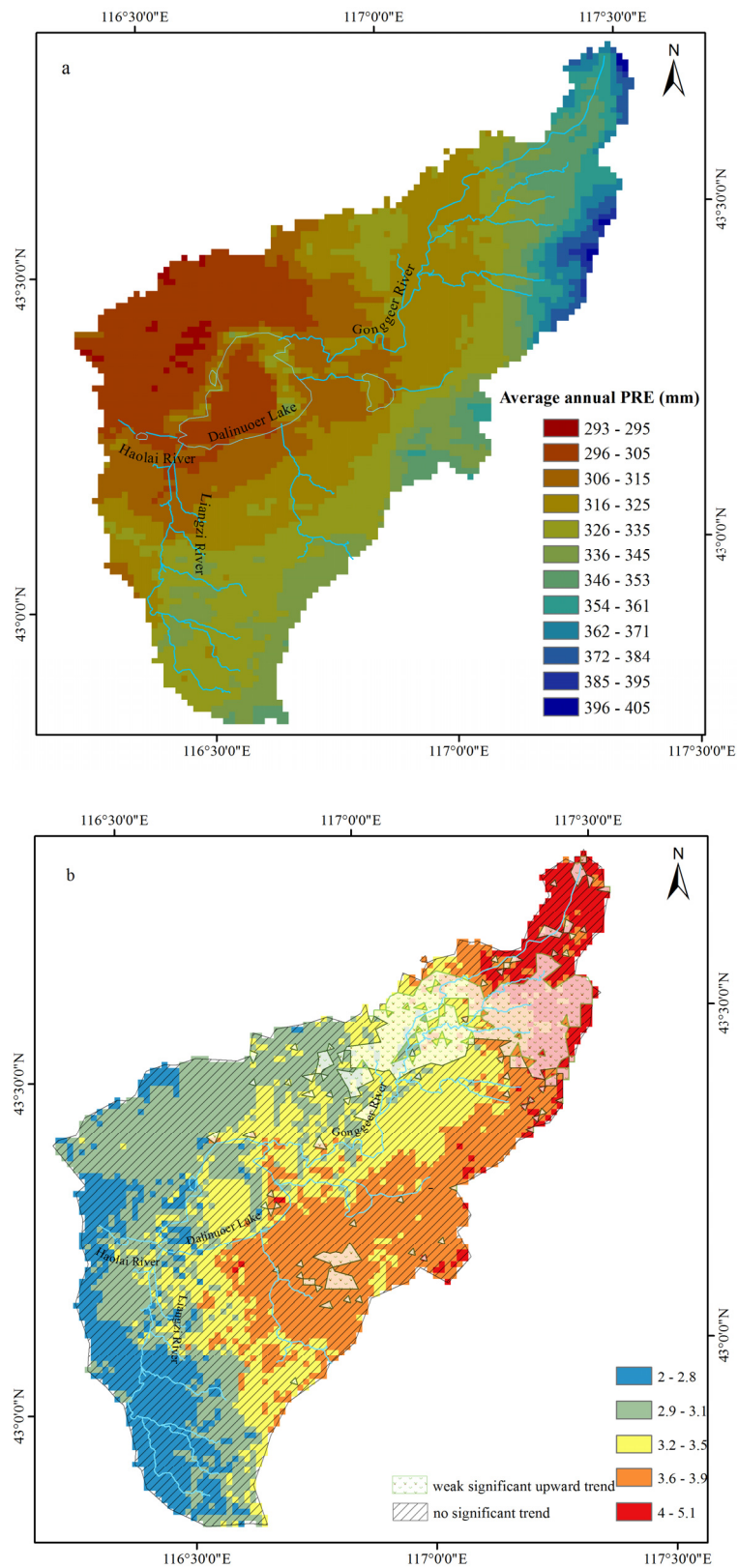**Figure 3.** Spatial distribution of annual inclination rate in the Dalinor Lake watershed from 2001 to 2019: PRE (**a**); AET (**b**); WD (**c**).

Figure 4. Spatial distribution of PRE from 2001 to 2019: average annual (**a**); the variation trends of annual PRE (**b**).
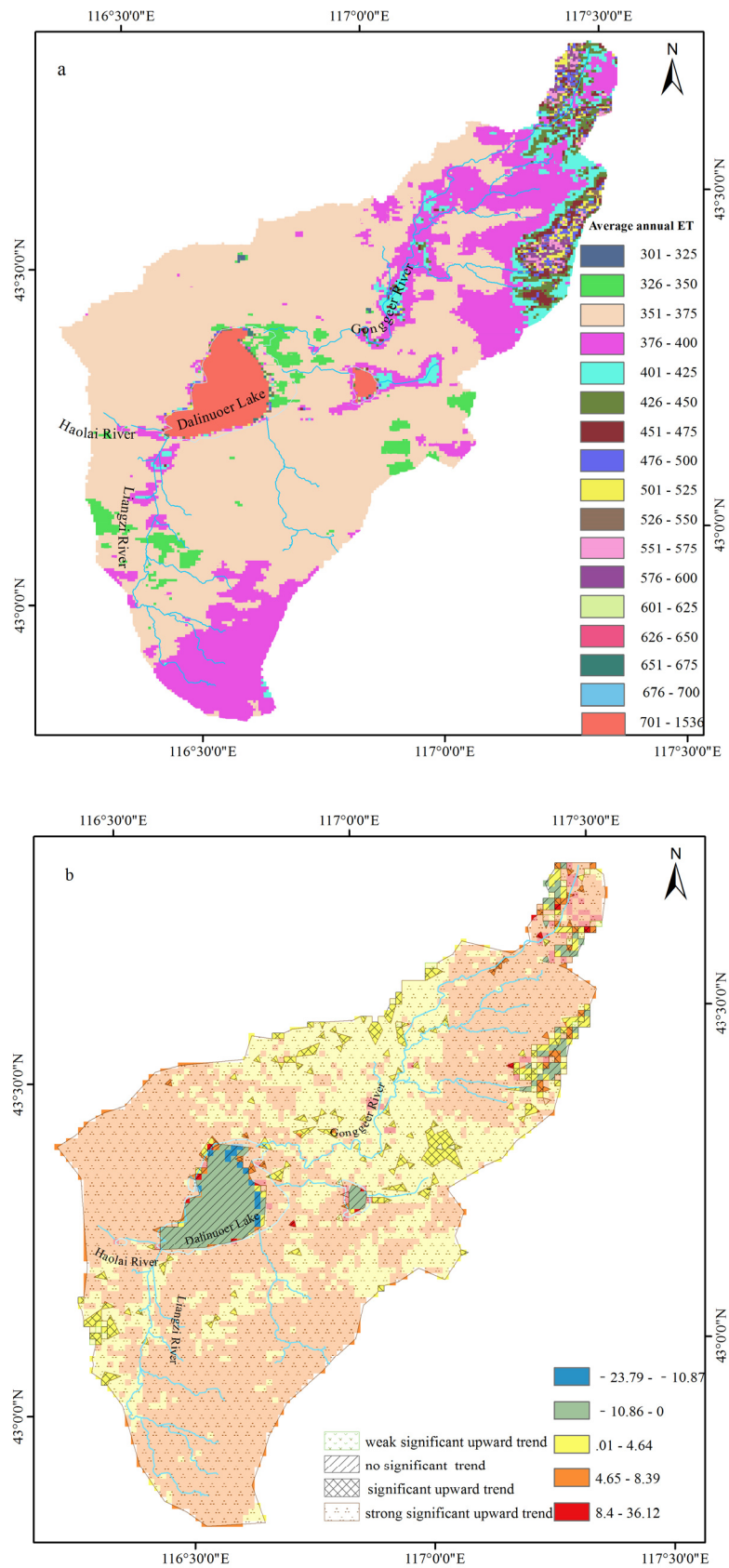
Figure 5. Spatial distribution of AET from 2001 to 2019: average annual AET (**a**); the variation trends of annual AET (**b**).

3.1.2. Actual Evapotranspiration

As shown in Figure 2, the trend of the annual AET in the Dalinor Lake watershed fluctuated between 371 mm/a and 480 mm/a from 2001 to 2019, with an average of 417 mm/a. From 2001 to 2019, annual AET showed a slowly increasing trend in fluctuation, with an increase rate of 4.13 mm/a, and the overall increase trend was statistically significant ($p < 0.05$). The variation coefficient of annual AET was 0.07, indicating weak inter-annual fluctuation. From the spatial distribution of the inclination rate, the spatial variation of the AET temporal trend varied greatly (Figure 3), ranging from −6.23 mm/10 a to 6.39 mm/10 a. The temporal trend of the AET showed an increasing trend for all the land use types except water evaporation.

As shown in Figure 4a, the average annual AET was between 139 and 1536 mm. The AET of the watershed had relatively strong spatial variations. Except for the waters area, the overall spatial distribution is high in the northeast and southwest parts of the watershed, as well as the riparian belt, the reason for which may be related to PRE, surface temperature, surface albedo, land use type, surface vegetation coverage, and other factors. Except for the waters area, the AET was mainly distributed in the ranges of 350–375 mm and 375–400 mm, accounting for 62.98% and 20.45%, respectively, among which the range of 375–400 mm was mainly distributed in the northeast, southwest, and riparian belt of the watershed. As shown in Figure 4b, the annual AET of Dalinor Lake showed an upward trend, except for a small part of the northeastern region. The upward trend was particularly obvious in the headwater region of the GongGeEr River, the riparian belt of the middle reaches of the GongGeEr River, and the southwestern and northwestern parts of Dalinor Lake. From a statistical point of view, about 89% of the watershed showed a very significant upward trend, and only 6% of the region showed no significant trend.

3.1.3. Water Surplus and Deficit

As shown in Figure 6, the trend of the annual WD in the Dalinor Lake watershed fluctuated between 20.18 mm/a and 214.72 mm/a from 2001 to 2019, with an average of 99 mm/a. From 2001 to 2019, annual WD showed a slowly increasing trend in fluctuation, with an increase rate of 0.71 mm/a, but it was not statistically significant ($p > 0.05$). The variation coefficient of annual WD is 0.48, indicating strong inter-annual fluctuation. From the spatial distribution of the inclination rate of WD (Figure 3), the spatial distribution varied greatly, ranging from −6.551 mm/10 a to 6.048 mm/10 a. From 2001 to 2019, the waters area and middle reaches of the GongGeEr River showed decreasing trend, while the other region basically showed an increasing trend.
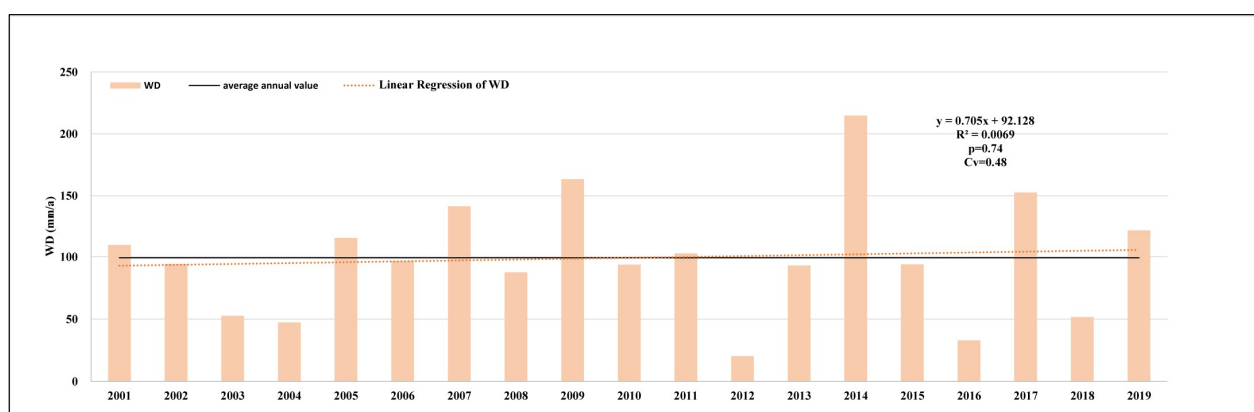

Figure 6. Inter-annual change in WD in the Dalinor Lake watershed from 2001 to 2019.

As shown in Figure 7a, the average value of the annual WD from 2001 to 2019 was between −10 mm and 1151 mm, with strong spatial variability. The overall spatial distribution was high in the northeast and low in the northwest in addition to the waters area, with a WD value up to 1151 mm. Moreover, 45.46% of the watershed with an annual WD value

between 40 and 60 mm was mainly distributed in the northeastern and northwestern parts of the watershed, as well as the middle reaches of the GongGeEr River. Furthermore, 27.34% of the watershed with an annual WD value between 60 and 80 mm was mainly distributed in the basalt zone located in the northwest and a small part of the northeast and southwest of the watershed. In addition, 4.70% of the watershed with an annual WD value between 80 and 120 mm was mainly distributed in a small part of the northeastern watershed and on both sides of the riparian belt. It can be seen from the spatial distribution of variation trends of annual WD in the Dalinor Lake watershed from 2001 to 2019 (Figure 7b) that the whole watershed showed an increasing trend except for a small part of the northeast. However, from a statistical point of view, about 98% of the watershed showed no significant increasing trend.
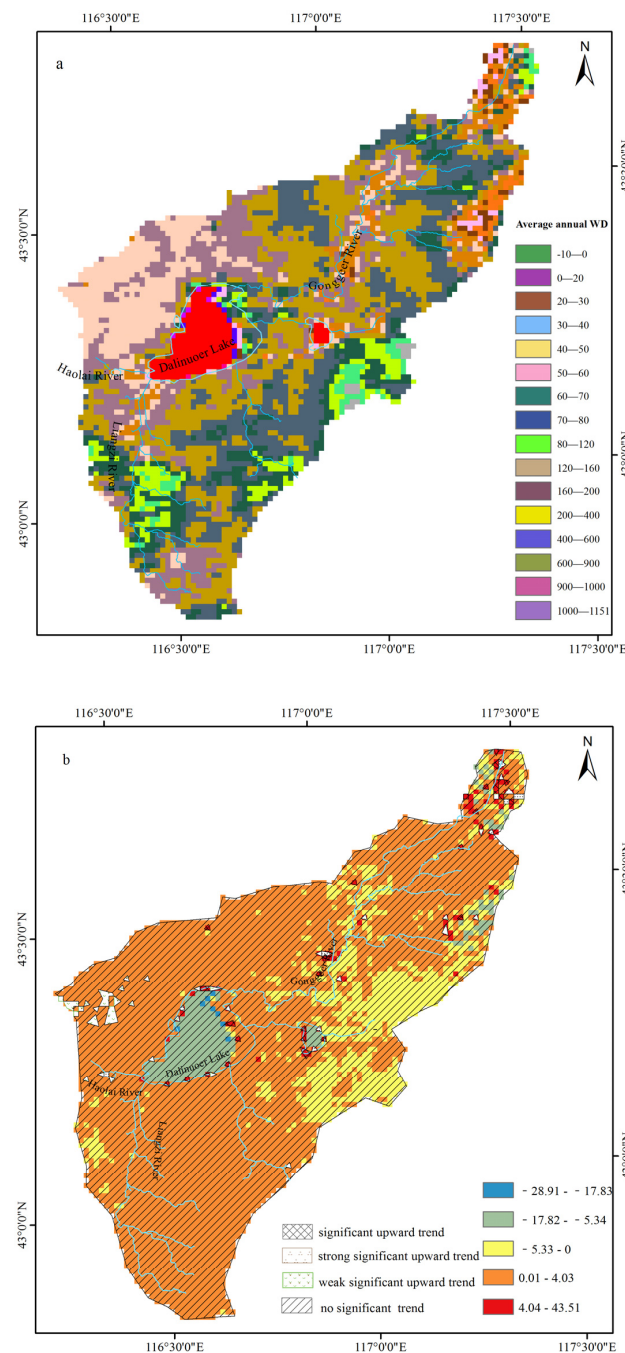

Figure 7. Spatial distribution of WD from 2001 to 2019: average annual WD (**a**); the variation trends of annual WD (**b**).

3.2. Land Use Changes in Different Lithological Zones

In the granite and terrigenous clastic rock zone, forest, grassland, and impervious land with areas of 149 km^2, 162 km^2, and 2 km^2, respectively, are mainly distributed (Figure 8a). From 2001 to 2019, the new total increased land use area in this zone was 44.34 km^2, among which 95.61% was forest (Figure 8b). It should be noted that the new increased farmland and impervious land converted from forest and grassland had also shown a slight increase, although it only accounted for 4.39% of the new total increased land use.
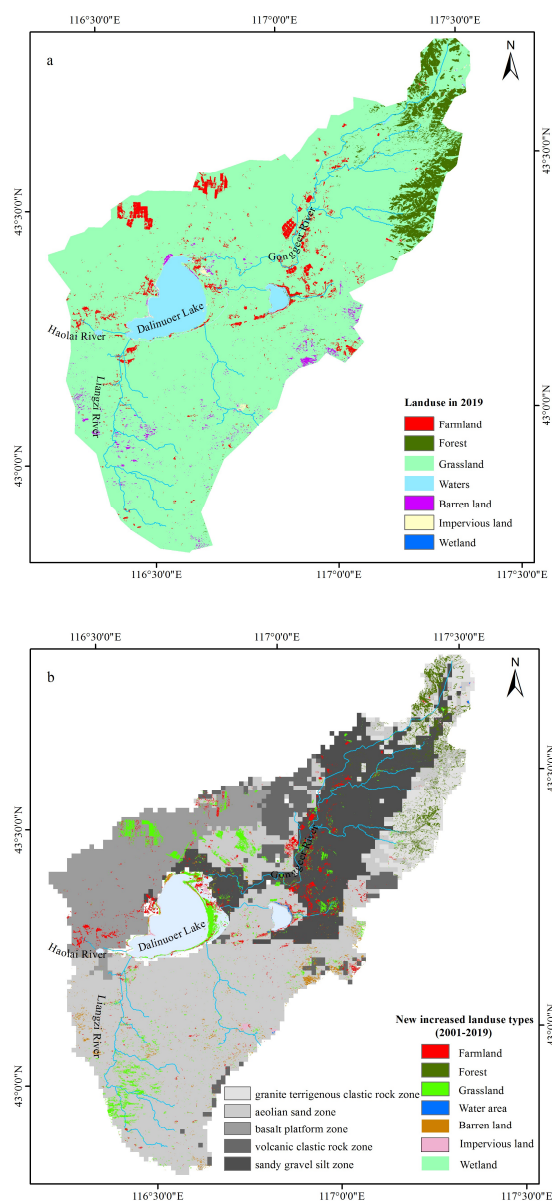
Figure 8. (**a**) Spatial distribution of the land use in 2019; (**b**) spatial distribution of the new increased land use from 2001 to 2019.

In the sand, gravel, and silt accumulation zone, grassland, farmland, forest, water area, and impervious area, with areas of 881 km^2, 35 km^2, 19 km^2, 6 km^2, and 2 km^2, respectively, were mainly distributed (Figure 8a). The area of the new increased farmland transferred from forest, grassland, and waters was 23.70 km^2 from 2001 to 2019, which accounted for 40.44% of the new total increased land use. The new increased farmland was mainly distributed on both sides of the riparian belt, corresponding with high vegetation coverage and greenness. The area of the new increased grassland transferred from farmland, forests,

waters, bare land, and wetland was 20.25 km^2 from 2001 to 2019, which accounted for 34.55% of the new total increased land use area. The area of the new increased forest transferred from farmland, grassland, and waters was 12.19 km^2 from 2001 to 2019, which accounted for 20.80% of the new total increased land use. It was sporadically distributed in the riparian belt of the upper reaches of the GongGeEr River (Figure 8b).

In the aeolian sand zone, grassland, farmland, forest, barren land, waters, and impervious area, with areas of 2159.92 km^2, 49.54 km^2, 43.42 km^2, 30.59 km^2, 22.57 km^2, and 2.93 km^2, respectively, were mainly distributed (Figure 8a). The area of the new increased grassland transferred from farmland, forests, waters, and bare land was 64.21 km^2 from 2001 to 2019, which accounted for 48.50% of the new total increased land use area. It was mainly distributed in the upper reaches of the Liangzi River and eastern Dalinor Lake. The area of the new increased farmland transferred from forest, grassland, waters, and barren land was 20.25 km^2 from 2001 to 2019, which accounted for 15.30% of the new total increased land use. The new increased grassland was mainly distributed between Dalinor Lake and Ganggennor Lake. The area of the new increased barren land with spotted sporadic distribution transferred from farmland, grassland, waters, and barren land was 18.04 km^2 from 2001 to 2019, which accounted for 13.63% of the new total increased land use. The area of the new increased forest land with spotted sporadic distribution transferred from grassland, farmland, and waters was 25.09 km^2 from 2001 to 2019, which accounted for 18.95% of the new total increased land use (Figure 8b).

In the basalt platform zone, grassland, farmland, waters, and bare land were mainly distributed, with areas of 685.25 km^2, 38.17 km^2, 1.93 km^2, and 0.35 km^2, respectively, in 2019 (Figure 8a). From 2001 to 2019, the area of the new increased grassland transferred from farmland, waters, and barren land was 21.36 km^2, which accounted for 77.59% of the new total increased land use. The area of the new increased farmland mainly transferred from grassland was 5.72 km^2 from 2001 to 2019, which accounted for 20.78% of the new total increased land use (Figure 8b).

3.3. The Water Surplus and Deficit Caused by Land Use Changes in Different Lithological Zones in the Dalinor Lake Watershed

3.3.1. Granite and Terrigenous Clastic Rock Zone

The WD caused by the new increased forest converted from farmland and grassland in 2019 was 4.6761 million m^3, which was reduced by 2.25 million m^3 compared with the same land use type in 2001. Forests are considered the most important ecosystems on land due to their conservation of soil water and groundwater recharge and their runoff regulation effect [48]. Although the forest could increase the AET, it did not lead to a WD increase due to the PRE increase; the forest may have been in a rising stage of water use efficiency. The per unit area of new increased farmland water consumption in 2019 was 472.21 mm, which was 1.14 times that of the same land use type in 2001. The per unit area of new increased impervious land water consumption in 2019 was 455.81 mm, which was 1.25 times that of the same land use type in 2001.

The granite and terrigenous clastic rock zone has the characteristics of less gravelly soil, good permeability, developed fissure water, and weak water storage capacity, with the maximum phreatic discharge reaching up to 100–1000 m^3/d, which is suitable for deep-rooted forest growth [49]. As mentioned above, the new increased land use type in the granite and terrigenous clastic rock zone was mainly forest. The forest can play an important role in windbreak, sand fixation, and water conservation. At present, the new increased forest did not lead to an increase in WD. However, it should be noted that the WD increased, caused by the increase in farmland and impervious land.

3.3.2. Sand, Gravel, and Silt Accumulation Zone

The WD caused by the new increased farmland in 2019 was 2.24 million m^3, which was increased by 0.016 million m^3 compared with the same land use type in 2001. The WD caused by the new increased grassland in 2019 was 2.33 million m^3, which was increased

by 0.10 million m^3 compared with the same land use type in 2001. The reason for the WD caused by the new increased grassland may be the expansion of artificial grassland to develop graziery. The WD caused by the new increased forest in 2019 was 1.32 million m^3, which was decreased by 0.26 million m^3 compared with the same land use type in 2001.

The sand, gravel, and silt accumulation zone is mainly composed of sand gravel and silty sand, with the characteristic of good water permeability, strong water storage capacity, shallow GW depth, and large phreatic discharge [49]. The new increased land use types in this zone were mainly farmland, grassland, and woodland. Although the riparian belt around the middle reaches of the GongGeEr River is suitable for crop cultivation, the river is also an important recharge source for Dalinor Lake [24]. As mentioned above, the WD caused by the new increased grassland was the largest, and the new increased farmland could also cause WD. The water yield would decrease as the WD increases, which would inevitably affect the health of the watershed ecosystem in the long run.

3.3.3. Aeolian Sand Zone

It was noteworthy that WD caused by the new increased land use in 2019 reached 10.62 million m^3, which accounted for 43.14% of the total WD of the Dalinor Lake watershed. The WD caused by the new increased grassland in 2019 was 4.45 million m^3, accounting for 41.92% of the total WD of the zone, which was increased by 2.23 million m^3 compared with the same land use type in 2001. It would be very likely that the expanded artificial grassland resulted in the increased WD in order to develop graziery.

The WD caused by the new increased farmland in 2019 was 1.97 million m^3, accounting for 18.52% of the total WD of the zone, which was increased by 4.45 million m^3 compared with the same land use type in 2001. The WD caused by the new increased barren land in 2019 was 0.62 million m^3, accounting for 5.9% of the total WD of the zone, which was increased by 0.20 million m^3 compared with the same land use type in 2001. As for the derelict land, the natural vegetation is difficult to recover, and the bare surface soil is vulnerable to wind erosion and desertification, and then becomes bare land. The WD caused by the new increased forest in 2019 was 2.92 million m^3, accounting for 20.69% of the total WD of the zone, which was decreased by 1.08 million m^3 compared with the same land use type in 2001.

The texture structure of the aeolian sand zone is sandy soil, with the lithology characteristics of good permeability and weak water storage capacity. Due to the aeolian sand underlying Quaternary loose rock, the GW depth is shallow, with a high discharge rate of 100–1000 m^3/d, which is conducive to the growth of shallow root vegetation grassland [49]. Moreover, affected by tectonic faults, spring water is outcropped to feed the Liangzi River, which flows into Dalinor Lake from the south [24]. The new increased land use types in the aeolian sand zone were mainly grassland, farmland, bare land, and forest. The high WD would lead to GW exploitation or spring-fed river interception to ensure farmland production and artificial grassland growth. The GW in this zone was an important recharge source of Dalinor Lake [24], and although in recent years, the shrinkage of Dalinor Lake has been alleviated, the local government should not blindly pursue surface runoff at the expense of GW. When the GW recharge is less than the discharge, it will disrupt the GW balance and decrease the GW storage. Then, a series of ecological problems will gradually emerge.

3.3.4. Basalt Platform Zone

The WD caused by the new increased grassland in 2019 was 1.94 million m^3, accounting for 73.70% of the total WD of the zone, which was increased by 0.45 million m^3 compared with the same land use type in 2001. The WD caused by the new increased farmland in 2019 was 0.52 million m^3, accounting for 19.87% of the total WD of the zone, which was increased by 0.15 million m^3 compared with the same land use type in 2001.

In the basalt platform zone, the lava platform, volcanic remnant cone, and mesa depression comprise the geomorphic unit; moreover, the SW system is not developed, and the GW recharged by PRE is mainly stored in the primary and secondary pores, fissures,

and clastic rocks of basalt [49]. The new increased land use types in this zone were mainly grassland and farmland, which led to the WD increase. The local people can only rely on GW exploitation to ensure farmland production and artificial grassland growth under the condition of no external water sources. It should be noted that in semi-arid regions, water resource endowment conditions are poor, PRE is rare, and GW recharge is limited. Once the GW recharge is less than the discharge, GW will be at risk of depletion. Hence, farmland reclamation and artificial grassland should be scientifically supervised.

3.4. Future Implications

Water resources play an important role in maintaining the ecological environment. The surface lithology zone has an obvious influence on water's ecological function. The ecological protection and territorial space planning should fully consider the regional surface lithology characteristics and functional zones of water resources. Firstly, it should be noted that the spring-fed river in the aeolian sand zone and the GongGeEr River in the sand, gravel, and silt accumulation zone are the important recharge sources of Dalinor Lake. Furthermore, the granite and terrigenous clastic rock zone is the important water yield region of the watershed. Secondly, although in recent years, the shrinkage of Dalinor Lake has been alleviated, in semi-arid regions, water resource endowment conditions are poor, PRE is rare, and GW recharge is limited. Once the GW recharge is less than the discharge, it will be at risk of depletion. The local government should not blindly pursue surface runoff at the expense of GW. Invisible GW should be given as much attention by local governments as visible SW. Thirdly, machine learning methods should be applied to further clarify the causes of ecological environment changes.

4. Conclusions

(1) In the past 20 years, the PRE and WD in the Dalinor Lake watershed showed insignificant upward trends, and the AET showed a significant upward trend. As for the spatial distribution of the trends of inter-annual PRE, the headwater of GongGeEr River and the southeastern part of Dalinor Lake showed a significant upward trend, and only the northeastern watershed surrounding the middle reaches of the GongGeEr River showed a weak significant upward trend. As for AET, about 89% of the watershed showed a significant upward trend. The headwater of GongGeEr River, the riparian belt near the middle reaches of the GongGeEr River, and the southwestern and northwestern parts of Dalinor Lake showed obvious upward trends. The WD of the watershed showed an overall upward trend, but the upward trend was not significant. The AET and WD in the riparian belt near the middle reaches of the GongGeEr River and the headwater of the Liangzi River showed high values, which may be caused by the increased farmland and artificial grassland.

(2) From 2001 to 2019, in the granite and terrigenous clastic rock zone, the new increased land use types were mainly forest, with a slight increase in farmland and industrial and mining land. In the sand, gravel, and silt accumulation zone, the new increased land use types were mainly farmland, grassland, and forest. In the aeolian sand zone, the new increased land use types were mainly grassland, farmland, impervious land, and forest. In the basalt platform zone, the new increased land use types were mainly grassland and farmland. Except for the increased forest, all the increased land use types resulted in the increase in WD. The increasing WD would lead to GW exploitation or spring-fed river interception to ensure farmland production and artificial grassland growth.

(3) In the future, it is necessary to strengthen the protection of regional forest ecosystems in the granite and terrigenous clastic rock zone; standardize pasture management and reduce farmland reclamation in the sand, gravel, and silt accumulation zone, the aeolian sand zone, and the basalt platform zone; and reduce unnecessary impervious land construction in the aeolian sand zone. Additionally, the relationship between economic development and environmental protection should be balanced at the watershed scale.

References

1. Sheng, Y. *Fresh Water and Watersheds*; CRC Press: Boca Raton, FL, USA, 2020; pp. 33–43.
2. Liu, X.; Yu, J.; Wang, P.; Zhang, Y.; Du, C. Lake evaporation in a hyper-arid environment, northwest of China—Measurement and estimation. *Water* **2016**, *8*, 527. [CrossRef]
3. Xu, C.-Y.; Chen, D. Comparison of seven models for estimation of evapotranspiration and groundwater recharge using lysimeter measurement data in Germany. *Hydrol. Process. Int. J.* **2005**, *19*, 3717–3734. [CrossRef]
4. Li, X.; Liu, S.; Xiao, Q.; Ma, M.; Jin, R.; Che, T.; Wang, W.; Hu, X.; Xu, Z.; Wen, J.; et al. A multiscale dataset for understanding complex eco-hydrological processes in a heterogeneous oasis system. *Sci. Data* **2017**, *4*, 170083. [CrossRef]
5. Wang, K.C.; Dickinson, R.E. A review of global terrestrial evapotranspiration: Observation, modeling, climatology, and climatic variability. *Rev. Geophys.* **2012**, *50*, RG2005. [CrossRef]
6. Angus, D.; Watts, P. *Developments in Agricultural and Managed Forest Ecology*; Elsevier: Amsterdam, The Netherlands, 1984; pp. 133–150.
7. Tanner, B.D. *Use Requirements for Bowen Ratio and Eddy Correlation Determination of Evapotranspiration*; ASCE: Reston, VA, USA, 1988; pp. 605–616.
8. Fisher, J.B.; Tu, K.P.; Baldocchi, D.D. Global estimates of the land–atmosphere water flux based on monthly AVHRR and ISLSCP-II data, validated at 16 FLUXNET sites. *Remote Sens. Environ.* **2008**, *112*, 901–919. [CrossRef]
9. Hemakumara, H.; Chandrapala, L.; Moene, A.F. Evapotranspiration fluxes over mixed vegetation areas measured from large aperture scintillometer. *Agric. Water Manag.* **2003**, *58*, 109–122. [CrossRef]
10. Fick, S.E.; Hijmans, R.J. WorldClim 2: New 1-km spatial resolution climate surfaces for global land areas. *Int. J. Climatol.* **2017**, *37*, 4302–4315. [CrossRef]
11. Xu, X. Yearly Spatial Interpolation Data Set of Meteorological Elements in China. Resource and Environment Science and Data Register and Publication System. 2022. Available online: http://www.resdc.cn/DOI (accessed on 3 August 2023).
12. Qu, L.; Zhu, Q.; Zhu, C.; Zhang, J. Monthly Precipitation Data Set with 1 km Resolution in China from 1960 to 2020. Science Data Bank. 2022. Available online: https://www.scidb.cn/en/cstr/31253.11.sciencedb.01607 (accessed on 3 August 2023).
13. Qin, R.; Zhao, Z.; Xu, J.; Ye, J.-S.; Li, F.-M.; Zhang, F. HRLT: A high-resolution (1 d, 1 km) and long-term (1961–2019) gridded dataset for surface temperature and precipitation across China. *Earth Syst. Sci. Data* **2022**, *14*, 4793–4810. [CrossRef]
14. Peng, S.; Ding, Y.; Liu, W.; Li, Z. 1 km monthly temperature and precipitation dataset for China from 1901 to 2017. *Earth Syst. Sci. Data* **2019**, *11*, 1931–1946. [CrossRef]
15. Mu, Q.; Zhao, M.; Running, S.W. Improvements to a MODIS global terrestrial evapotranspiration algorithm. *Remote Sens. Environ.* **2011**, *115*, 1781–1800. [CrossRef]
16. Chen, M.; Senay, G.B.; Singh, R.K.; Verdin, J.P. Uncertainty analysis of the Operational Simplified Surface Energy Balance (SSEBop) model at multiple flux tower sites. *J. Hydrol.* **2016**, *536*, 384–399. [CrossRef]
17. Senay, G.B.; Friedrichs, M.; Morton, C.; Parrish, G.E.; Schauer, M.; Khand, K.; Kagone, S.; Boiko, O.; Huntington, J. Mapping actual evapotranspiration using Landsat for the conterminous United States: Google Earth Engine implementation and assessment of the SSEBop model. *Remote Sens. Environ.* **2022**, *275*, 113011. [CrossRef]
18. Elnashar, A.; Wang, L.; Wu, B.; Zhu, W.; Zeng, H. Synthesis of global actual evapotranspiration from 1982 to 2019. *Earth Syst. Sci. Data* **2021**, *13*, 447–480. [CrossRef]

19. Zhang, Y.; Kong, D.; Gan, R.; Chiew, F.H.S.; McVicar, T.R.; Zhang, Q.; Yang, Y. Coupled estimation of 500 m and 8-day resolution global evapotranspiration and gross primary production in 2002–2017. *Remote Sens. Environ.* **2019**, *222*, 165–182. [CrossRef]

20. Yang, J.; Huang, X. The 30 m annual land cover dataset and its dynamics in China from 1990 to 2019. *Earth Syst. Sci. Data* **2021**, *13*, 3907–3925. [CrossRef]

21. Chen, J.; Chen, J.; Liao, A.; Cao, X.; Chen, L.; Chen, X.; He, C.; Han, G.; Peng, S.; Lu, M.; et al. Global land cover mapping at 30 m resolution: A POK-based operational approach. *ISPRS J. Photogramm. Remote Sens.* **2015**, *103*, 7–27. [CrossRef]

22. Zhang, X.; Liu, L.; Chen, X.; Gao, Y.; Xie, S.; Mi, J. GLC_FCS30: Global land-cover product with fine classification system at 30 m using time-series Landsat imagery. *Earth Syst. Sci. Data* **2021**, *13*, 2753–2776. [CrossRef]

23. Xu, L.; Gao, G.; Wang, X.; Chen, Y.; Zhou, C.; Wang, K.; Fu, B. Quantifying the contributions of climate change and human activities to vegetation greening in the drylands of northern China. *Acta Ecol. Sin.* **2023**, *828*, 1–10. (In Chinese)

24. Li, W.; Wang, L.; Zhang, Y.; Wu, L.; Zeng, L.; Tuo, Z. Determining the groundwater basin and surface watershed boundary of Dalinuoer Lake in the middle of Inner Mongolian Plateau, China and its impacts on the ecological environment. *China Geol.* **2021**, *4*, 498–508.

25. Xing, Z.; Huang, H.; Li, Y.; Liu, S.; Wang, D.; Yuan, Y.; Zhao, Z.; Bu, L. Management of sustainable ecological water levels of endorheic salt lakes in the Inner Mongolian Plateau of China based on eco-hydrological processes. *Hydrol. Process.* **2021**, *35*, e14192. [CrossRef]

26. Tao, S.; Fang, J.; Zhao, X.; Zhao, S.; Shen, H.; Hu, H.; Tang, Z.; Wang, Z.; Guo, Q. Rapid loss of lakes on the Mongolian Plateau. *Proc. Natl. Acad. Sci. USA* **2015**, *112*, 2281–2286. [CrossRef] [PubMed]

27. Bai, M.; Mo, X.; Liu, S.; Hu, S. Detection and attribution of lake water loss in the semi-arid Mongolian Plateau—A case study in the Lake Dalinor. *Ecohydrology* **2020**, *14*, e2251. [CrossRef]

28. Bao, Y.; Ren, J. Wetland Landscape Classification Based on the BP Neural Network in DaLinor Lake Area. *Procedia Environ. Sci.* **2011**, *10*, 2360–2366. [CrossRef]

29. Bao, Y.; Zhang, X. The study of lakes dynamic change based on RS and GIS—Take DaLiNuoEr Lake as an example. *Procedia Environ. Sci.* **2011**, *10*, 2376–2384. [CrossRef]

30. Li, H.; Gao, Y.; Li, Y.; Yan, S.; Xu, Y. Dynamic of Dalinor Lakes in the Inner Mongolian Plateau and Its Driving Factors during 1976–2015. *Water* **2017**, *9*, 749. [CrossRef]

31. Jiang, X.; Liu, C.; Hu, Y.; Shao, K.; Tang, X.; Zhang, L.; Gao, G.; Qin, B. Climate-induced salinization may lead to increased lake nitrogen retention. *Water Res.* **2023**, *228*, 119354. [CrossRef] [PubMed]

32. Zhen, Z.; Li, W.; Xu, L.; Zhang, X.; Zhang, J. Lake-level variation of Dali Lake in mid-east of inner Mongolia since the Late Holocene. *Quat. Int.* **2021**, *583*, 62–69. [CrossRef]

33. Yu, E.; Cui, N.; Quan, Y.; Wang, C.; Jia, T.; Wu, D.; Wu, G. Ecological protection for natural protected areas based on landsenses ecology: A case study of Dalinor National Nature Reserve. *Int. J. Sustain. Dev. World Ecol.* **2020**, *27*, 709–717. [CrossRef]

34. Zheng, Z.; Yang, Z.; Chen, Y.; Wu, Z.; Marinello, F. The Interannual Calibration and Global Nighttime Light Fluctuation Assessment Based on Pixel-Level Linear Regression Analysis. *Remote. Sens.* **2019**, *11*, 2185. [CrossRef]

35. Montgomery, D.C.; Peck, E.A.; Vining, G.G. *Introduction to Linear Regression Analysis*; John Wiley & Sons: Hoboken, NJ, USA, 2021.

36. Hijmans, R.J.; Bivand, R.; Forner, K.; Ooms, J.; Pebesma, E.; Sumner, M.D. *Package 'Terra'*; Maintainer: Vienna, Austria, 2022.

37. Theil, H. A rank-invariant method of linear and polynomial regression analysis. *Indag. Math.* **1950**, *12*, 173.

38. Sen, P.K. Estimates of the regression coefficient based on Kendall's tau. *J. Am. Stat. Assoc.* **1968**, *63*, 1379–1389. [CrossRef]

39. Hoaglin, D.C.; Mosteller, F.; Tukey, J.W. Understanding robust and exploratory data analysis. In *Wiley Series in Probability and Mathematical Statistics*; Wiley: Hoboken, NJ, USA, 1983.

40. Sayemuzzaman, M.; Jha, M.K. Seasonal and annual precipitation time series trend analysis in North Carolina, United States. *Atmos. Res.* **2014**, *137*, 183–194. [CrossRef]

41. Jiang, W.; Yuan, L.; Wang, W.; Cao, R.; Zhang, Y.; Shen, W. Spatio-temporal analysis of vegetation variation in the Yellow River Basin. *Ecol. Indic.* **2015**, *51*, 117–126. [CrossRef]

42. Kendall, M. *Rank Correlation Methods*; Charles Griffin: London, UK, 1975.

43. Tošić, I. Spatial and temporal variability of winter and summer precipitation over Serbia and Montenegro. *Theor. Appl. Clim.* **2004**, *77*, 47–56. [CrossRef]

44. Pohlert, T. *Trend: Non-Parametric Trend Tests and Change-Point Detection 2018*; The R Project for Statistical Computing: Vienna, Austria, 2018.

45. Huang, H.; Zhou, Y.; Qian, M.; Zeng, Z. Land Use Transition and Driving Forces in Chinese Loess Plateau: A Case Study from Pu County, Shanxi Province. *Land* **2021**, *10*, 67. [CrossRef]

46. Liu, F.; Qin, T.; Girma, A.; Wang, H.; Weng, B.; Yu, Z.; Wang, Z. Dynamics of Land-Use and Vegetation Change Using NDVI and Transfer Matrix: A Case Study of the Huaihe River Basin. *Pol. J. Environ. Stud.* **2018**, *28*, 213–223. [CrossRef]

47. Miao, L.; Zhang, C.; Wang, Y.; He, S.; Han, Y.; Li, X.; Zhang, X. The Effects of Land Usage on Water Balance in the Sandy Areas in Horqin of Inner Mongolia. *J. Irrig. Drain.* **2021**, *40*, 106–113. (In Chinese)

48. Krishnaswamy, J.; Bonell, M.; Venkatesh, B.; Purandara, B.K.; Rakesh, K.; Lele, S.; Kiran, M.; Reddy, V.; Badiger, S. The groundwater recharge response and hydrologic services of tropical humid forest ecosystems to use and reforestation: Support for the "infiltration-evapotranspiration trade-off hypothesis". *J. Hydrol.* **2013**, *498*, 191–209. [CrossRef]
49. Wei, X.; Wang, J.; Sun, H.; Yin, Z.; He, Z.; Jia, F.; Li, X.; Liu, H.; Zhang, J. Exploration of land use optimization path based on geological formation in Chengde City. *Hydrogeol. Eng. Geol.* **2020**, *47*, 15–25.